

Diffusion and Filtration Properties of Self-Assembled Gold Nanocrystal Membranes

Jinbo He,[†] Xiao-Min Lin,[‡] Henry Chan,[§] Lela Vuković,[§] Petr Král,[§] and Heinrich M. Jaeger^{*,†}

[†]James Franck Institute, University of Chicago, Chicago, Illinois 60637, United States

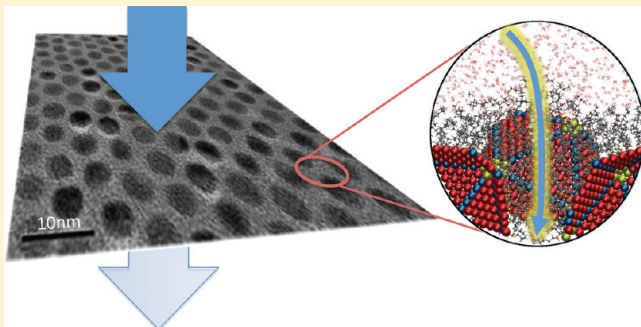
[‡]Center for Nanoscale Materials, Argonne National Laboratory, Argonne, Illinois 60439, United States

[§]Department of Chemistry, University of Illinois at Chicago, Chicago, Illinois 60607, United States

 Supporting Information

ABSTRACT: Close-packed nanoparticle monolayers have recently been shown to form mechanically robust, free-standing membranes. We report the first measurements of molecular transport through such ultrathin sheets, self-assembled from dodecanethiol-ligated gold nanocrystals. For aqueous solutions we find filtration coefficients 2 orders of magnitude larger than those observed in polymer-based filters, sieving of large solutes, and for smaller solutes a pronounced dependence of rejection on being charged. These results open up new possibilities for controlled delivery and separation of nano-objects.

KEYWORDS: Nanoparticle, self-assembly, membranes, diffusion, filtration



For increased nanofiltration performance, and in particular higher throughput at lower applied pressure, reduction of the filter thickness is advantageous.^{1–4} However, reaching the limit of a few nanometers is difficult when mechanical robustness and tightly controlled pore size are also required. Here we introduce a new ultrathin membrane that achieves this. It consists of sheets of well-ordered ligand-coated metal nanocrystals that are draped over a microfiltration disk for mechanical support. We use simple drying-mediated self-assembly, which is known to produce sheets that are strong mechanically and can be suspended over holes up to micrometers across.^{5–8} In filters formed from monolayers of 5 nm diameter gold nanocrystals with dodecanethiol ligand shells, we find filtration coefficients (volume flux/pressure) around 10^{-6} m/(s·kPa) for aqueous solutions, ~100 times larger than in typical polymer-based nanofiltration systems. At only ~82 kPa pressure across the membrane, the membranes exhibit pronounced charge sensitivity for a variety of dyes and other molecules with effective cross section <1.6 nm: rejection is 45–60% for charged molecules compared to ~10% when they are uncharged. Objects with cross section >1.7 nm are rejected completely. Guided by atomistic molecular dynamics simulations, we propose that molecular transport occurs through porelike regions of reduced ligand density in the interstices between close-packed nanocrystals and that dielectric exclusion dominates the charge-dependent rejection.

Figure 1a shows a typical image of a monolayer of dodecanethiol-ligated gold nanocrystals (5.0 ± 0.5 nm in diameter; see Figure S1 in the Supporting Information for a histogram), self-assembled on the surface of a water drop and imaged by transmission electron microscopy (TEM) after drying. The

one-step drying method results in a well-ordered, close-packed particle sheet that can drape itself over solid substrates⁹ as well as across holes.^{5–8} For a given particle type and size, the ligands establish a characteristic interparticle spacing and provide for mechanical strength of the assembly.⁷ In typical nanofiltration membranes transport occurs through 0.5–2 nm diameter pores or channels, while reverse osmosis membranes are based on diffusion through polymeric networks.¹⁰ Well-defined open pores do not exist in close-packed nanocrystal assemblies because the ligands extend into the interstices (Figure 1c). In panels a–c of Figure 1 the distances between nanocrystals directly facing each other are of similar size as the length of the dodecanethiol (≈ 1.7 nm), which implies not only a dense but also a highly interdigitated ligand arrangement in those regions. However, in the center of triangles formed by three neighboring particles, the ligands are packed less densely (more chain ends, less interdigitation) and this makes these regions the most likely spots for molecular passage (white circle in Figure 1c). Clearly, transport will be blocked for molecules that cannot fit at all into the interstices between neighboring particles. The question we focus on here is what happens for aqueous solution of somewhat smaller molecules.

In general, transport through a membrane can be described as arising from two contributions, diffusion due to concentration gradients and convection due to pressure gradients.¹¹ As a first step to ascertain the relative magnitude of the two terms, we determine

Received: March 13, 2011

Revised: May 1, 2011

Published: May 06, 2011

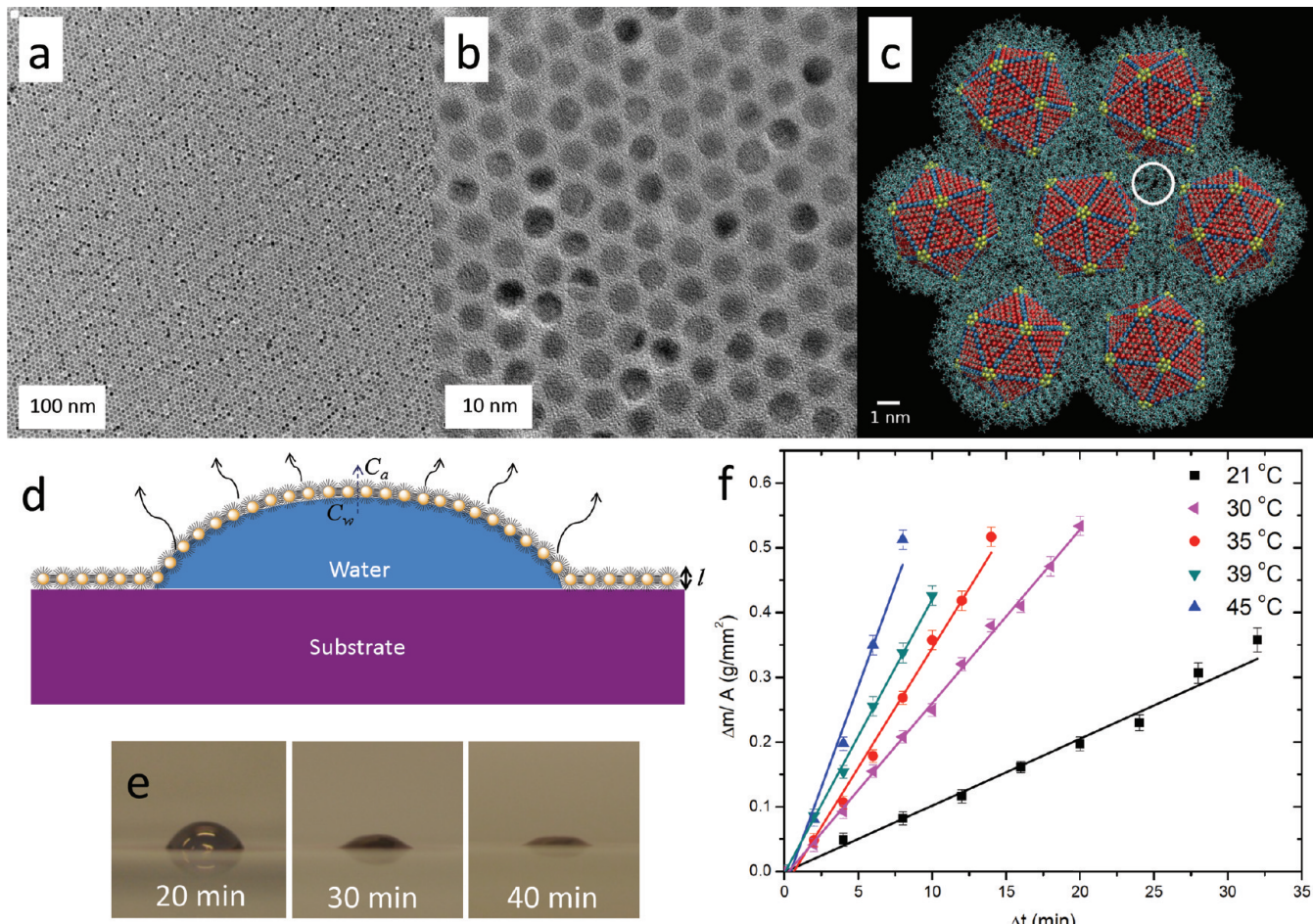


Figure 1. Self-assembled nanoparticle monolayers. (a) Transmission electron microscopy (TEM) image of monolayer of dodecanethiol-coated gold nanocrystals, self-assembled by a one-step drying method. (b) TEM with higher magnification detail of the close-packed nanoparticle arrangement. (c) Snapshot from an atomistic simulation of the nanocrystal layer. Image shows a regular lattice; effects of disorder and fluctuations are discussed in the Supporting Information. For clarity, water molecules are not depicted. (d) Schematic view (in cross section) of the drop drying process. After nanoparticle-containing solution (in toluene) has been applied to the top of a water droplet, the solution quickly spreads and, after evaporation of the solvent, forms a nanoparticle monolayer that completely covers the water droplet while it dries. (e) Images of the covered water droplets at different drying times. (f) Mass loss Δm of the water droplet as a function of time interval Δt . Here Δm is normalized by the drop surface area A (at time t). $\Delta t = 0$ corresponds to the point in time when the nanoparticle monolayer has fully formed and enveloped the water droplet. The lines represent best fits. See the Supporting Information for a discussion of the temperature dependence of the mass loss and the resulting activation energy.

the water flux J_D due to diffusion through the nanoparticle sheet, using the droplet drying process itself. As the data in Figure 1d–f show, water droplets covered with a nanoparticle monolayer evaporate much slower than bare droplets. The monolayer membrane forms during evaporation of the nanoparticle solvent (toluene) at the early stage of drying. After that, it completely covers the whole water drop. Measurement of the mass loss Δm during the subsequent water evaporation therefore provides direct access to the permeability $P = DS$, i.e., the product of diffusivity, D , and solubility, S , via $J_D = \Delta m/(A\rho\Delta t) = DS/l$. Here A is the surface area of the droplet, ρ the water density, l the monolayer thickness (≈ 8.4 nm for a 5 nm diameter gold core plus two layers of ligands), and Δt the time after monolayer formation. If we account for the fact that the area shrinks during drying and compute $A(\Delta t)$ from images of the evolving drop shape (Figure 1e), we find that $\Delta m/A$ grows linearly with time, corresponding to a $J_D \approx 1.7 \times 10^{-6}$ m/s under ambient conditions (21 °C). Given that $\approx 55\%$ of the area of our nanoparticle monolayers is taken up by gold particles, this leads

to $P_{\text{ligand}} \approx 3 \times 10^{-11}$ g/(cm·s) for the water permeability through the interstices. To estimate the diffusivity we express $S = C_w - C_a$ as the difference between the water concentrations at the water (C_w) and air (C_a) sides of the membrane. Since the water evaporates to open air, $C_a \approx 0$. For C_w we take the solubility of water in dodecane,¹² 4.83×10^{-5} g/cm³, which is a good approximation since the thiol groups are attached to gold surfaces. This gives $D \approx 6 \times 10^{-7}$ cm²/s, a diffusion coefficient similar to that for water diffusing in low density polyethylene¹³ and at least a factor 100 larger than in aromatic polyamide membranes used for desalination.¹⁴

In order to measure the flux under an applied differential pressure, we incorporate the Au nanoparticle membranes into a nanofiltration unit as shown in Figure 2. It consists of nanoparticle monolayers prepared by drop drying, transferred onto a polycarbonate filter disk for mechanical support (Figure 2a,b). This type of filter disk (Whatman Cyclopore) contains 100 nm diameter pores (see Figure S3 in the Supporting Information for AFM characterization) over which the nanocrystal layers drape

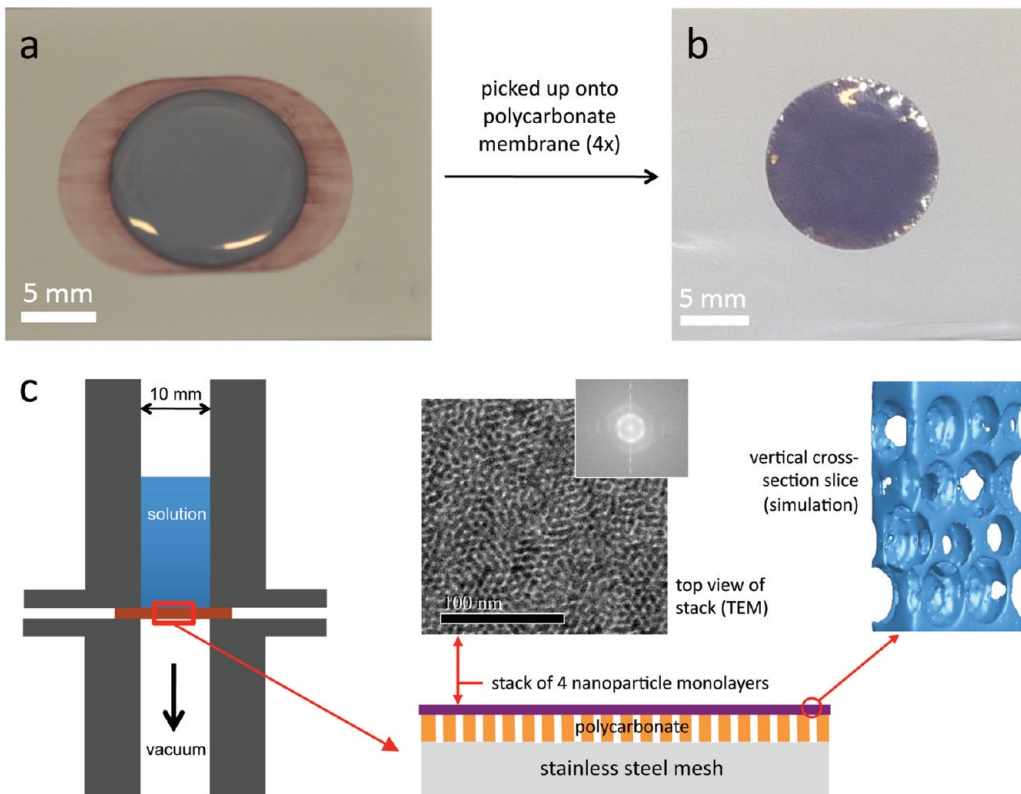


Figure 2. Nanoparticle-based filter. (a) Optical image of a 13 mm diameter water droplet covered with a gold nanoparticle membrane that is one monolayer thin. (b) Polycarbonate filter covered by a stack of four gold nanoparticle membranes, fabricated by lifting monolayers from drops as shown in panel a. The polycarbonate contains larger holes, 100 nm in diameter. (c) Cross section of the device used for the filtration experiments. Zoomed-in sketch shows nanoparticle membrane stack on top of polycarbonate filter and stainless steel mesh for mechanical support. The TEM image is a view through the four-membrane stack (inset: computed diffraction pattern), while the computer simulation visualizes a cross-sectional slice. The rendered volume is accessible to solvent (blue), while empty spherical portions represent the inaccessible volume (nanoparticle cores plus 1 nm shell accounting for the region of most densely packed ligands). In the simulation, four layers of Lennard-Jones spheres with diameter distribution as in the experiments were prepared and equilibrated separately at $T = 300$ K, then stacked on top of each other with random relative orientations but only briefly equilibrated.

themselves, forming membranes that cover the pores. To mitigate the effect of occasional defects, such as particle vacancies, dislocations, or grain boundaries, additional layers were deposited on top of the first. In our study, stacks of four monolayers were found to be sufficiently robust and defect tolerant (total membrane thickness $L = 4l \approx 34$ nm). We note that, since individual layers in the stack are deposited sequentially, they are not in registry with each other. Consequently, even in a four layer thick membrane there is a significant probability for (nearly) vertical passage through much of the stack, as demonstrated by the multitude of bright spots in the TEM image of such stack in Figure 2c. Since TEM images do not show the ligands and cannot directly indicate the network of interconnected pathways available to the aqueous solution, in Figure 2c the accessible interstitial space between nanoparticles is visualized by showing a 3D vertical slice through a simulated four-layer stack. In this simulation spherical particles with the same size distribution as in the experiments were used, but the effective particle size was increased such that the average pore diameter in the equatorial plane of each layer corresponds to that of the white circle in Figure 1c. As already seen in the TEM image, passage is not blocked in a multilayer stack and typical pathways span top to bottom by meandering sideways no more than a few nanometers.

The polycarbonate disk with the four-layer nanoparticle membrane stack was placed on a stainless steel mesh in the

filtration unit, a 82 kPa pressure differential ΔP was applied by pulling a vacuum downstream (Figure 2c), and the resulting total flux J was measured. For aqueous solutions, the filtration coefficient $J/\Delta P$, i.e., the ratio of water flux through the active area of the membrane (given by the area occupied by the 100 nm pores, roughly 3% of the total) to pressure drop, was $\approx 1 \times 10^{-6}$ m/(s·kPa). Such large filtration coefficient, 2 orders of magnitude bigger than for typical polymer-based membranes,¹⁵ is a direct consequence of the nanoscale thickness of the membrane.

For a variety of dyes and larger fluorescent molecules with weights ranging from 200 to 43000 and charge states from +1 to -4 the filter performance was measured by comparing the permeate concentration, C_p , to that of the feeding solution, C_f , determining both by spectroscopy from the peak intensities in the UV–Vis spectra (Figure S5, Supporting Information). Figure 3 shows the rejection, $R = 1 - C_p/C_f$, as a function of the effective diameter d of the smallest cross section of each molecule. For ovalbumin and water-soluble Au nanoparticles (see Figure S4 in the Supporting Information for a TEM image), both with $d \geq 2$ nm, rejection was >99%. Below a cutoff near 1.6 nm, the nanocrystal filter exhibits strikingly little size or shape sensitivity, or dependence on the particular charge state of the solute, except that when charge is present, rejection jumps to 45–60% from $\approx 10\%$ for uncharged species. In both cases the size cutoff is remarkably sharp, clearly demonstrating the absence

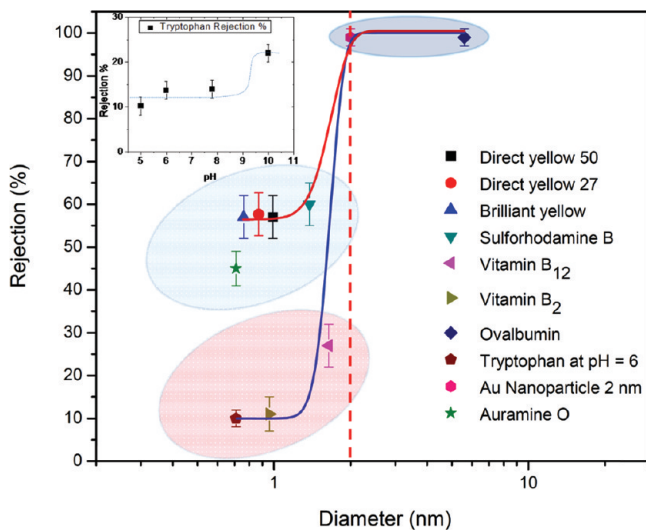


Figure 3. Nanofiltration performance. Rejection R is plotted as a function of the diameter d of the smallest cross section of each molecule. Data for molecular species with a wide molecular weight range, shape, and charge state are shown, as indicated by the legend (see Supporting Information for a detailed listing). The oval shaded areas show total rejection for objects larger than 1.7 nm in diameter (gray), ~10% rejection of smaller uncharged species (light blue), and 45–60% rejection for smaller charged species (pink). The red dashed line represents the diameter of the circle drawn in Figure 1c, indicating the upper limit of pore size predicted by standard pore flow models. The red and blue lines are predictions from a model for $R(d)$ based on sieving, as explained in the text. In this model, nanopores result from low ligand density regions in the interstices and the width of the transition in $R(d)$ is determined by small variations in the diameter of the nanoparticles. The lines correspond to a mean pore diameter $d_p = 1.65$ nm and a pore diameter spread $\sigma_p = 0.25$ nm, in line with TEM analysis of the nanoparticle diameter variation. To account for the effects of residual steric hindrance and for dielectric exclusion of the charged species, diameter-independent offsets were allowed for $R(d)$. This approach does not consider the shape of the solute; of the charged species tested only Auramine O is the most compact and spherical, which could be the reason for its lower R value. The inset shows the rejection of tryptophan at different pH values.

of significant defects in the membrane stack and ruling out transport through any type of larger holes.

How do solute molecules move through the membrane and what is the relative magnitude of the diffusive and convective contributions? To elucidate this, we performed atomistic molecular dynamics simulations of the relative free energy profiles, $\Delta G(z)$, using an adaptive biasing force method^{16–18} (see Supporting Information for details). As shown in Figure 1c, each nanocrystal is modeled as an icosahedral shell covered by dodecanethiol (one ligand per three surface gold atoms). The unit cell has flexible boundaries, allowing lateral fluctuations of the membrane. To address the effect of charge, the passage of tryptophan was simulated for three cases, corresponding to three pH conditions: zwitterion ($-\text{NH}_3^+$, $-\text{COO}^-$), neutral ($-\text{NH}_2$, $-\text{COOH}$), and negatively charged ($-\text{NH}_2$, $-\text{COO}^-$). In Figure 4 we plot $\Delta G(z)$ as a function of distance, z , of the solute molecule from the midplane of the nanoparticle monolayer for trajectories through the center of the white circle shown in Figure 1c. The energy difference, $\Delta\Delta G = \Delta G(z)|_{z=4\text{ nm}} - \Delta G(z)|_{z=0}$, between outside and midway inside the membrane is negative in all cases, indicating the solubility is higher in water than in the alkane

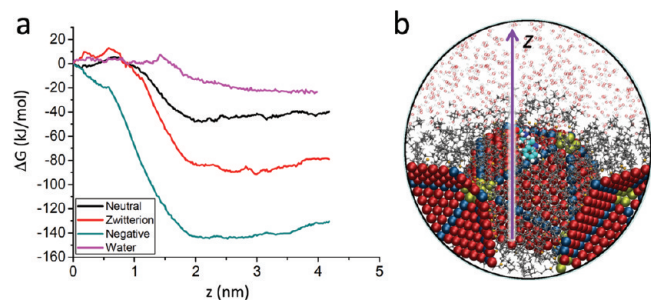


Figure 4. Atomistic simulations of solutes approaching the membrane from the interface with bulk water. (a) Free energy profiles, $\Delta G(z)$, are shown for water (pink) and different charge states of tryptophan (neutral, black; zwitterion, red; negative, blue), as a function of the distance, z , between the solute and the midplane of the membrane ($z = 0$). Bulk water corresponds to the region $z > 4$ nm. The solute approaches the membrane along a trajectory that goes through a 3-fold coordinated interstitial site (center of dashed red circle in Figure 1c). As a result of the wide mouth of a pore at this location, the solute interacts with the alkane environment only at close approach ($z < 2$ nm). (b) Cutaway view of a tryptophan molecule (blue and white) moving toward the “pore” region formed between three gold nanoparticles, each modeled as an icosahedral shell (red atoms on the faces, blue atoms along the edges, and yellow atoms at the vertices). Dodecanethiol chains as well as water molecules are shown. Parts of the system in front of the tryptophan are excluded for clarity.

environment of the membrane. Already for nonionized tryptophan the fact that $\Delta\Delta G$ is found to be roughly twice the value for water would imply exceedingly small passage rates. For the charged species the solubility barrier is even higher, predicting a rejection much larger than the roughly 5-fold increase for R seen in the experiments when compared to the uncharged species (Figure 3). Furthermore, in experiments using tryptophan where we increased the pH to ≈ 10 , just over pK_{a2} , so that 70–80% of the molecules were negatively charged, R only doubled (Figure 3 inset).

These results imply that transport is unlikely to occur by diffusion through interstices that are as densely filled with ligands as simulated under equilibrium conditions for a perfectly regular nanoparticle lattice (Figure 1c). Instead, they point to a mechanism driven by convective pore flow. Porelike regions can occur for a variety of reasons, even if the particles are in a well-ordered, close-packed arrangement. Besides the possibility that ligands reorganize dynamically during the solute passage (something our simulations did not include), other factors are small variations in particle size and position, and temperature-driven fluctuations (for a discussion, see Supporting Information and Figures S6 and S7). A picture of transport dominated by convective pore flow is also supported by the measured water flux J which, at $\Delta P = 82$ kPa through a stack of four layers, was about 82×10^{-6} m/s or almost 50 times larger than the flux J_D from self-diffusion through a single monolayer. Thus, $J \approx J_C$, where J_C is the flux due to pressure-driven convection.

How big would the pores have to be to account for the measured flux? Certainly the holes visible in Figure 1c are too small (the atomistic simulation did not account for rearrangement of the ligands during flow or a distribution of nanocrystal diameters). To obtain an effective pore diameter, d_p , we use the standard expression¹⁰ $J_C = \varepsilon \pi d_p^2 \Delta P / (32 \mu L)$, where ε is the surface porosity, μ the water viscosity, and L the pore channel length. Taking $L = 4l \approx 34$ nm for the four-layer membrane and

assuming that each nanocrystal is surrounded by six pores, i.e., $\varepsilon = (6\pi d_p^2/4)/(3\sqrt{3}/2s^2)$, where $s = 6.7$ nm is the average center-to-center spacing for our dodecanethiol-coated Au particles, we find $d_p \approx 1.7$ nm. If instead only 50% of the possible pores were actually open, d_p would increase by a factor $2^{1/4}$ to ≈ 2.0 nm (the diameter of the white circle in Figure 1c). Without the need to assume a modified water viscosity inside the pore,³ this range of d_p values is in excellent agreement with the cutoff diameter for molecular passage seen in Figure 3.

However, certain aspects of the data point to differences with typical models for pore flow. A first aspect is the steplike behavior of $R(d)$ we observe. Usually, a variety of hindrance factors, describing the interaction of the solute with the solvent inside the pore as well as with the pore geometry, start to contribute to rejection well before the ratio $\lambda = d/d_p$ approaches unity, producing a much more gradual increase. For ultrathin nanocrystal monolayer membranes, it instead appears that, at least to first approximation, all solutes with diameter d smaller than the effective size of a given pore can pass through equally well, with the key difference being whether or not they are charged. We attribute this to the fact that the ligands are tethered with one end to the nanocrystals, resulting in hour-glass-shape pores with wide entrance and exit regions and a short bottleneck around $z=0$. In this scenario the shape of $R(d)$ simply reflects the cumulative bottleneck size distribution.¹¹ For a Gaussian distribution this implies $R \sim 1 + \text{erf}[(d - d_p)/(\sqrt{2}\sigma_p)]$, where $\text{erf}(x)$ is the error function, d_p is the mean bottleneck diameter, and σ_p its standard deviation. If we assume that σ_p is primarily due to variation in nanoparticle diameters, $d = (5.0 \pm 0.5)$ nm as determined by TEM analysis (Figure S1, Supporting Information), and that the stack of nanoparticle membranes acts like four sieves in series, we can set $\sigma_p = 0.5 \text{ nm}/\sqrt{4} = 0.25 \text{ nm}$ and find that $R(d)$ should follow the curves given by the solid lines in Figure 3, in very good agreement with the data (see Supporting Information for more details). The bottleneck size $d_p \approx 1.65$ nm obtained from a best fit to the rejection data is the same for charged and uncharged solutes.

A second difference arises from the finding that solute charges from +1 to -4 give rather similar values for R . This is in contrast to typical polymer-based nanofiltration membranes where a combination of electric (Donnan) and dielectric effects implies that highly charged species are rejected more strongly.¹⁰ Our nanocrystal sheets are not charged, which makes the dominant mechanism dielectric exclusion, i.e., the repulsion of charged solutes due to image charges of the same sign that build up at interfaces of significant dielectric contrast, such as the water/ligand interface inside the pore.^{19–22} In our system the channels are sufficiently narrow that the charged solute ions travel together with counterions,²¹ resulting in an independence of R on the charge state.^{19,20,22} Nevertheless, polarization of the metal nanoparticles might be thought to counteract this repulsion by producing image charges that attract solute ions. However, penetration of the electric field into the metal needs to be accounted for and, as a result, even in fully metallic membranes dielectric exclusion is expected to dominate for pore sizes <4 nm.²³

Our findings demonstrate that nanoparticle sheets combine several desirable characteristics for nanofiltration, namely, strong size and charge selectivity at low pressure, with ease of fabrication offered by drying-mediated self-assembly. Since the membranes form into close-packed monolayers at an air–liquid interface far away from any substrate and since they exhibit exceedingly small

bending stiffness before they have dried, they can be draped over surfaces of arbitrary topography or shape, as demonstrated by the fact that they easily conform, without rupture, to predeposited electrodes⁹ or deep steps etched into in SiN.^{7,8} With improved processing, it should in principle be possible to provide filtration down to the extreme limit of single, ~ 10 nm thin monolayers. Furthermore, different particle–ligand combinations could be used to control the pore size.^{5,7} This makes them promising candidates for applications not only for nano-filtration and separation but also for controlled delivery and encapsulation.^{24–26}

■ ASSOCIATED CONTENT

S Supporting Information. Detailed experimental methods for preparation and characterization of nanoparticle membranes and procedures for filtration, as well as molecular dynamic simulations. This material is available free of charge via the Internet at <http://pubs.acs.org>.

■ AUTHOR INFORMATION

Corresponding Author

*E-mail: h-jaeger@uchicago.edu.

■ ACKNOWLEDGMENT

We thank Scott Waitukaitis for help with the image analysis and Benjamin Duval for building the holder for the filtration devices. We thank Yitzhak Rabin, Tom Witten, Cynthia Jameson, and Dmitri Talapin for many fruitful discussions. This work was supported by the NSF through DMR-0907075 and CBET-0932812. The Chicago MRSEC, supported by NSF under DMR-0820054, is gratefully acknowledged for access to its shared experimental facilities. The work at Argonne was supported by the U.S. Department of Energy (DOE), BES-Materials Sciences, under Contract #DE-AC02-06CH11357, and by the DOE Center for Nanoscale Materials. The simulations were performed in part on NCSA, CNM, and NERSC computer networks.

■ REFERENCES

- (1) Holt, J. K.; Noy, A.; Huser, T.; Eaglesham, D.; Bakajin, O. *Nano Lett.* **2004**, *4*, 2245.
- (2) Striemer, C. C.; Gaborski, T. R.; McGrath, J. L.; Fauchet, P. M. *Nature* **2007**, *445*, 749.
- (3) Peng, X. S.; Jin, J.; Nakamura, Y.; Ohno, T.; Ichinose, I. *Nat. Nanotechnol.* **2009**, *4*, 353.
- (4) Hinds, B. J.; Chopra, N.; Rantell, T.; Andrews, R.; Gavalas, V.; Bachas, L. G. *Science* **2004**, *303*, 62.
- (5) Cheng, W. L.; Campolongo, M. J.; Cha, J. J.; Tan, S. J.; Umbach, C. C.; Muller, D. A.; Luo, D. *Nat. Mater.* **2009**, *8*, 519.
- (6) Dong, A. G.; Chen, J.; Vora, P. M.; Kikkawa, J. M.; Murray, C. B. *Nature* **2010**, *466*, 474.
- (7) He, J.; Kanjanaboons, P.; Frazer, N. L.; Weis, A.; Lin, X.-M.; Jaeger, H. M. *Small* **2010**, *6*, 1449.
- (8) Mueggenburg, K. E.; Lin, X. M.; Goldsmith, R. H.; Jaeger, H. M. *Nat. Mater.* **2007**, *6*, 656.
- (9) Tran, T. B.; Beloborodov, I. S.; Lin, X. M.; Bigioni, T. P.; Vinokur, V. M.; Jaeger, H. M. *Phys. Rev. Lett.* **2005**, *95*, 076806.
- (10) Baker, R. W. *Membrane technology and applications*; McGraw-Hill: New York, 2000.
- (11) Otero, J. A.; Mazarrasa, O.; Villasante, J.; Silva, V.; Pradanos, P.; Calvo, J. I.; Hernandez, A. *J. Membr. Sci.* **2008**, *309*, 17.
- (12) Schatzberg, P. J. *Phys. Chem.* **1963**, *67*, 776.

- (13) Schatzberg, P. *J. Polym. Sci., Part C: Polym. Symp.* **1965**, *10*, 87.
- (14) Razumovskii, L. P.; Markin, V. S.; Zaikov, G. Y. *Polymer Science U.S.S.R.* **1985**, *27*, 341.
- (15) Akthakul, A.; Salinaro, R. F.; Mayes, A. M. *Macromolecules* **2004**, *37*, 7663.
- (16) Darve, E.; Pohorille, A. *J. Chem. Phys.* **2001**, *115*, 9169.
- (17) Darve, E.; Rodriguez-Gomez, D.; Pohorille, A. *J. Chem. Phys.* **2008**, *128*, 144120.
- (18) Henin, J.; Chipot, C. *J. Chem. Phys.* **2004**, *121*, 2904.
- (19) Saliha, B.; Patrick, F.; Anthony, S. *Chem. Eng. Sci.* **2009**, *64*, 3789.
- (20) Szymczyk, A.; Fievet, P. *J. Membr. Sci.* **2005**, *252*, 77.
- (21) Kamenev, A.; Zhang, J.; Larkin, A. I.; Shklovskii, B. I. *Phys. A (Amsterdam, Neth.)* **2006**, *359*, 129.
- (22) Rabin, Y.; Tanaka, M. *Phys. Rev. Lett.* **2005**, *94*, 148103.
- (23) Kornyshev, A. A. *Sov. Electrochem.* **1988**, *24*, 385.
- (24) Chan, H.; Kral, P. *Nanoscale* **2011**, *3*, 1881.
- (25) Lin, Y.; Skaff, H.; Emrick, T.; Dinsmore, A. D.; Russell, T. P. *Science* **2003**, *299*, 226.
- (26) Russell, J. T.; Lin, Y.; Boker, A.; Su, L.; Carl, P.; Zettl, H.; He, J. B.; Sill, K.; Tangirala, R.; Emrick, T.; Littrell, K.; Thiagarajan, P.; Cookson, D.; Fery, A.; Wang, Q.; Russell, T. P. *Angew. Chem., Int. Ed.* **2005**, *44*, 2420.